The Astrophysical Journal, 999:196 (13pp), 2026 March 10 https://doi.org/10.3847/1538-4357/ae401f

On the Thermal and Magnetic Properties of an Active Region Jet

Chunyu Ji[1], Jiajia Liu[1,2], Wensi Wang[2], Zhenyong Hou[3], Xianyong Bai[4,5,6], and Yuming Wang[1,2]
[1] National Key Laboratory of Deep Space Exploration, School of Earth and Space Sciences, University of Science and Technology of China, Hefei 230026, People's Republic of China; jiajialiu@ustc.edu.cn
[2] CAS Center for Excellence in Comparative Planetology/CAS Key Laboratory of Geospace Environment/Mengcheng National Geophysical Observatory, University of Science and Technology of China, Hefei 230026, People's Republic of China
[3] School of Earth and Space Sciences, Peking University, Beijing 100871, People's Republic of China
[4] State Key Laboratory of Solar Activity and Space Weather, National Astronomical Observatories, Chinese Academy of Sciences, Beijing 100101, People's Republic of China
[5] School of Astronomy and Space Sciences, University of Chinese Academy of Sciences, Beijing 100049, People's Republic of China
[6] Institute for Frontiers in Astronomy and Astrophysics, Beijing Normal University, Beijing 102206, People's Republic of China
Received 2025 November 27; revised 2026 January 25; accepted 2026 January 30; published 2026 March 3

Abstract

Jets, as an essential manifestation of the release of the free magnetic energy, are ubiquitous in the solar atmosphere. We present a comprehensive analysis of a multithermal blowout jet that occurred in active region AR 13102 on 2022 September 20, using observations from the Solar Dynamics Observatory (SDO)/Atmospheric Imaging Assembly, SDO/Helioseismic and Magnetic Imager (HMI), Interface Region Imaging Spectrograph, and Solar Upper Transition Region Imager. The jet is initiated by compact brightenings at its footpoints and exhibits a curtain-like spire with apparent rotational and weak lateral whipping motions. Time–distance analysis reveals a projected axial velocity $\sim$300 km s^{-1} and a rotational speed $\sim$30 km s^{-1}. Differential emission measure analysis shows that the jet plasma spans a broad temperature range, with hot ($\gtrsim$10 MK) plasma concentrated near the flare loops and jet base and cooler components extending along the spire. Using the derived kinetic and thermal properties, we conclude that there is an equipartition between the jet's kinetic energy $(5.4 \pm 2.4) \times 10^{20}$ J and thermal energy $(7.0 \pm 3.6) \times 10^{20}$ J. HMI vector magnetograms and nonlinear force-free field extrapolations reveal that the jet originates from a compact mixed-polarity region at the edge of the active region, where flux emergence and cancellation, a low-lying twisted magnetic flux rope with a maximum twist number of $\sim$2.1, and a surrounding high-Q quasi-separatrix layer are present. The observed decrease in twist after the eruption, together with the jet's untwisting, indicates that the jet is driven by the eruption and the reconnection of the twisted flux rope, converting magnetic free energy into plasma heating and bulk motion. Our results highlight the importance of small-scale flux rope eruptions in driving blowout jets and releasing twist through magnetic reconnection and untwisting motions.

Unified Astronomy Thesaurus concepts: Solar activity (1475); Solar corona (1483); Solar chromosphere (1479); Solar magnetic reconnection (1504)

Materials only available in the online version of record: animation

1. Introduction

Solar jets are transient energy release phenomena commonly observed in the solar atmosphere, manifesting as collimated plasma beams ejected from the solar surface (K. Shibata et al. 1992; Y. Shen 2021). As a crucial bridge connecting small-scale magnetic activity with large-scale coronal dynamics, jet research holds significant importance for understanding key scientific issues such as coronal heating and solar wind acceleration (e.g., K. Shibata et al. 2007; H. Tian et al. 2014; R. Lionello et al. 2016; T. Samanta et al. 2019; G. Wu et al. 2025). The typical velocity of jets ranges from 10 to 1000 km s^{-1}, with an average around 200 km s^{-1} (M. Shimojo et al. 1996). Their spatial length scales range from tens of thousands to several hundred thousand kilometers, with durations lasting from a few minutes to several tens of minutes (J. Cirtain et al. 2007; N. K. Panesar et al. 2023). Solar jets exhibit a wide range of plasma temperatures, reflecting their complex energy release and heating processes. Observations have revealed that Hα jets correspond to relatively cool plasma with temperatures of approximately 10^4 K (K. Shibata et al. 2007; Y. Qi et al. 2022; G. Wu et al. 2025), while extreme-ultraviolet (EUV) jets are formed in the transition region and low corona at temperatures of about 10^5–10^6 K (R. Harrison et al. 2001; G. Nisticò et al. 2009; S. Anfinogentov et al. 2021; A. Sahay et al. 2023). In contrast, X-ray jets are associated with hot coronal plasma (typically a few $\times$ 10^6 K, with some events reaching up to $\sim 10^7$ K; M. Shimojo et al. 1996; J. Cirtain et al. 2007; D. E. Innes et al. 2016; I. Loboda et al. 2025). These phenomena collectively demonstrate the multithermal nature of solar jets (e.g., J. Liu et al. 2016; X. Li et al. 2025a), which generally contain both cool ($\sim 10^4$ K) and hot components ($\sim 10^6$ K or higher). According to some theories and observations, the cool component mainly originates from a small eruptive filament confined near the jet base (e.g., A. C. Sterling et al. 2015; Y. Shen et al. 2017; R. L. Moore et al. 2018; J. Wang et al. 2024; S. Tan et al. 2025), whereas the hot component represents plasma that has been significantly heated and accelerated during the magnetic reconnection process (T. Yokoyama & K. Shibata 1995; Y. Shen et al. 2017; Y. Zhang et al. 2023). Currently, multiwavelength imaging observations with high temporal and spatial resolution provide a more comprehensive understanding of the thermal structure and dynamic evolution of solar jets. Spectroscopic observations reveal the rotational and untwisting motions of jets,

typically characterized by simultaneous blueshift and redshift signatures on opposite sides of the jet axis (e.g., C. Pike & H. Mason 1998; J. Liu et al. 2014; M. C. Cheung et al. 2015; J. Liu et al. 2017; L. Lu et al. 2019; N. K. Panesar et al. 2022, 2025).

Based on morphology and dynamics, solar jets can be classified into standard and blowout jets. Standard jets are produced by magnetic reconnection between closed magnetic loops and the surrounding open magnetic field, typically exhibiting a simple, narrow, and well-collimated structure without significant twist. In contrast, blowout jets originate from the eruption of a sheared or twisted base arch that contains a minifilament or flux rope, resulting in a broader and more complex morphology (R. L. Moore et al. 2010, 2013; T. K. Baikie et al. 2022; A. C. Sterling et al. 2022). Both types of jets are driven by magnetic reconnection processes; however, the fundamental distinction lies in the eruption behavior of the embedded minifilament, with successful filament eruptions giving rise to blowout jets, whereas failed or absent filament eruptions are associated with standard jets. Blowout jets are commonly associated with a jet bright point (JBP; P. R. Young & K. Muglach 2014; N. K. Panesar et al. 2016a; A. C. Sterling et al. 2017; A. Bura et al. 2025). Studies by N. K. Panesar et al. (2016b) and A. C. Sterling et al. (2016) indicate that minifilament eruptions are triggered by flux cancellation at the underlying neutral line, and a JBP appears on the neutral line in the wake of the erupting minifilament. Magnetic flux cancellation (e.g., Y. Jiang et al. 2007; C. Chifor et al. 2008; N. K. Panesar et al. 2016b; J. Liu et al. 2023b; S. Patsourakos & V. Archontis 2025) or flux emergence (e.g., M. J. Murray et al. 2009; F. Moreno-Insertis & K. Galsgaard 2013; F. Fang et al. 2014; L. Yang et al. 2017; X. Li et al. 2023, 2025b) in the lower solar atmosphere can modify the local magnetic topology, such as the fan–spine configuration (e.g., S. Masson et al. 2009; P. F. Wyper et al. 2017; Y. Duan et al. 2024; A. Bhatnagar et al. 2025), leading to magnetic instability and reconnection that rapidly releases stored magnetic energy. When a minifilament or a twisted flux rope is present, its eruption and upward expansion can further initiate reconnection and produce high-speed plasma ejections along open magnetic field lines. Some jets exhibit untwisting or whiplike motions, which are interpreted as the outward propagation of torsional Alfvén or kink waves that transport magnetic energy and helicity (R. Moll et al. 2008; M. Hoshino & K. Higashimori 2015; B. Schmieder 2022; J. Touresse et al. 2024). Overall, the eruption of solar jets is a multiscale process involving magnetic energy accumulation, instability, and release through 3D magnetic reconnections.

Many studies have extensively investigated solar jets in coronal holes and quiet-Sun regions, where the magnetic configuration is relatively simple and dominated by open magnetic fields (K. Chandrashekhar et al. 2014; N. Narang et al. 2016; S. Mandal et al. 2022; V. Upendran et al. 2025). These studies have established that magnetic reconnection between open and closed field lines, often triggered by flux emergence or cancellation, serves as the primary driving mechanism for coronal jets. However, jets in active regions (ARs) remain relatively underexplored, particularly those with small spatial scales and intermittent recurrence. Compared with coronal hole or quiet-Sun jets, AR jets are characterized by stronger and more complex magnetic fields, higher plasma temperatures, and more dynamic multithermal structures. The magnetic environment in ARs adds complexity to the initiation and evolution of jets, making it difficult to determine the exact role of magnetic topology in jet initiation. Recent high-resolution observations and modeling show that many AR jets are driven by the eruption of small-scale flux ropes/minifilaments and can release magnetic twist that propagates outward along reconnecting fields; notably, a subset of AR jets exhibit "hidden-onset" behavior in which the pre-eruptive core is difficult to detect because of projection/temperature effects in strong-field regions (Y. Shen 2021; P. Kayshap et al. 2024). In addition, new transition region imaging from Solar Upper Transition Region Imager (SUTRI) provides improved constraints on flows and heating at jet footpoints, enabling better assessment of TR–corona coupling and energy/mass closure in AR jets (X. Bai et al. 2023). Nevertheless, systematic large-sample studies that quantitatively close the thermal, kinetic, and magnetic (torsional) energy budgets across different triggering scenarios remain scarce, leaving the detailed physics of AR jet initiation and twist transport an open question (Y. Shen 2021; D. M. Long et al. 2023).

In this work, we present a detailed analysis of the magnetic field configuration and energy evolution associated with an AR jet, revealing how magnetic energy is accumulated and subsequently released to drive the jet eruption. The multithermal nature of the jet is also studied in detail. This analysis leverages state-of-the-art observations, including those in the rarely detected transition region lines from China's first solar transition region telescope, SUTRI (X. Bai et al. 2023). Furthermore, we provide a comprehensive interpretation of the relationship among the rotational motion, the release of magnetic twist, and the underlying magnetic conditions at the jet base. The structure of this paper is organized as follows: Section 2 describes the datasets and observations. Section 3 presents the results obtained from the differential emission measure (DEM) analysis of the event. Section 4 discusses the evolution of energy fluxes and the magnetic topology. We summarize our work in Section 5.

2. Data and Observations

In this study, data from the Atmospheric Imaging Assembly (AIA; J. R. Lemen et al. 2012) and the Helioseismic and Magnetic Imager (HMI; P. H. Scherrer et al. 2012) on board the Solar Dynamics Observatory (SDO; W. D. Pesnell et al. 2012), the Slit Jaw Imager (SJI; B. De Pontieu et al. 2014) of the Interface Region Imaging Spectrograph (IRIS), and SUTRI (X. Bai et al. 2023) were used to investigate a jet event in AR 13102 during the period from 15:00 UT to 16:00 UT on 2022 September 20. SDO/AIA provides EUV images at wavelengths of 94, 131, 171, 193, 211, 304, and 335 Å with a time interval of 12 s and a pixel scale of $0\farcs6$, which are used to diagnose the structural characteristics of the jet plasma in the transition region and at coronal temperatures. SDO/HMI provides photospheric continuum intensity maps at a 45 s cadence and vector magnetograms at a 12-minute cadence, both with a $0\farcs5$ pixel scale. The simultaneously acquired IRIS SJI images employed in this research cover three wavelength bands (C II λ1330, Si IV λ1400, and Mg II k λ2796) with a pixel size of $0\farcs33$, providing observations of the upper chromosphere and transition region. SUTRI is China's first solar transition region telescope, on board the Space Advanced Technology demonstration satellite-01 (SATech-01) of the Chinese Academy of Sciences (CAS). Launched in 2022 July, it operates in a Sun-synchronous orbit at an altitude of ~500 km with an orbital period of 96 minutes. SUTRI observes the Ne VII 46.5 nm

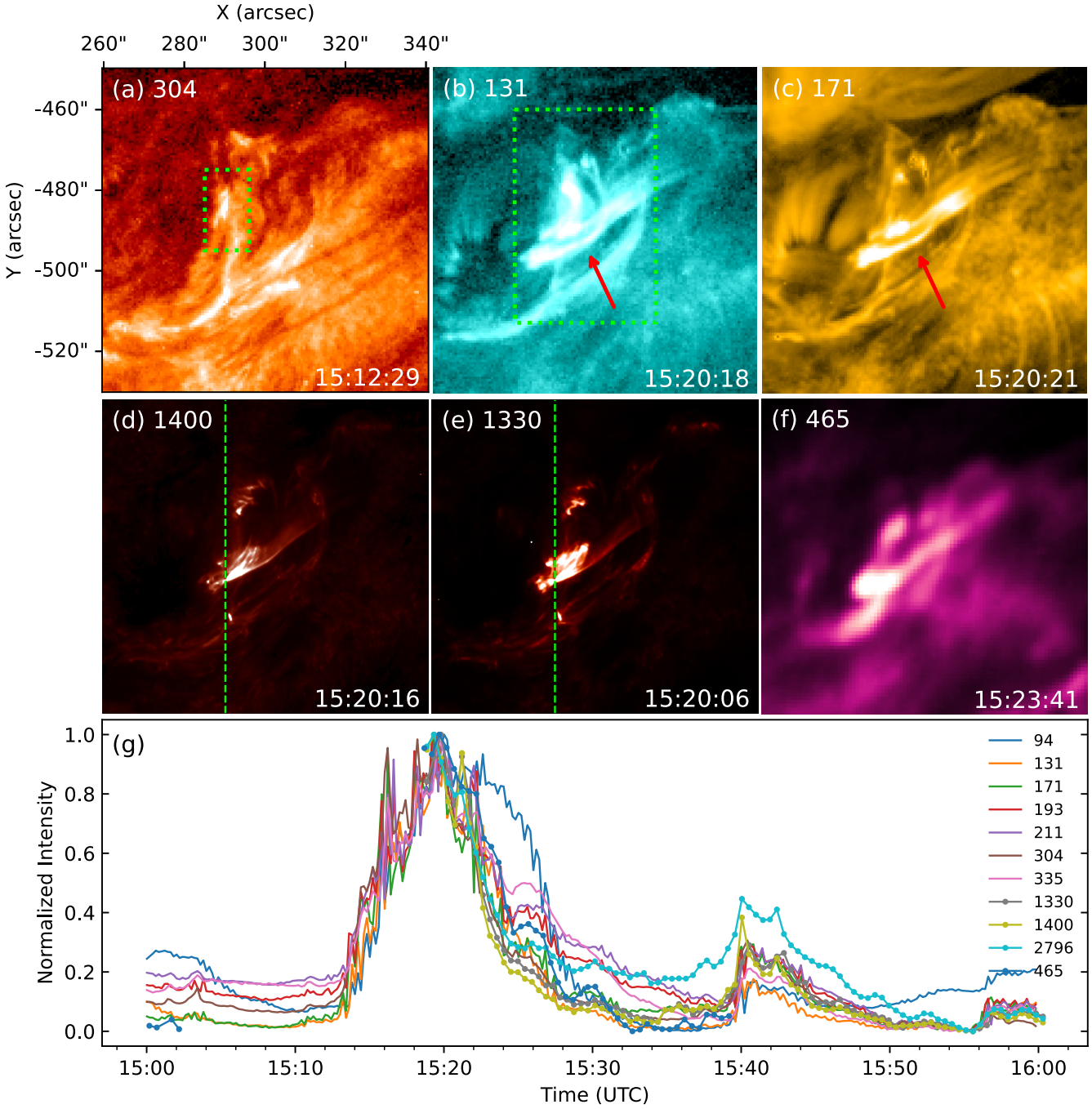

Figure 1. SDO/AIA EUV (panels (a)–(c)), IRIS/SJI far-UV (panels (d) and (e)), and SUTRI (panel (f)) observation of the jet in AR 13102 around 15:12–15:23 UT on 2022 September 20. (g) Temporal evolution of the normalized average intensity within the green dashed box in panel (b) at seven SDO/AIA passbands, three IRIS/SJI passbands, and one SUTRI passbands. The green dashed box in panel (a) highlights the first appearance of the bright point in the jet footpoint region. The green dashed box in panel (b) surrounds the main body of the jet, as well as the footpoint region, with the red arrow pointing to the jet. In panels (d) and (e), the green dashed lines represent the positions of the slit in the IRIS sit-and-stare mode. An animation showing the jet formation with the same field of view as the panel (a) still image is provided. The animation starts at 15:10:05 UT and ends at 15:30:05 UT, corresponding to the first jet event and lasting 30 minutes.

(An animation of this figure is available in the online article.)

spectral line, which forms in the solar transition region at a temperature of ∼0.5 MK. It features a spatial resolution of 8″ and a temporal resolution of 30 s and captures full-disk images in a 2048 × 2048 pixel^2 format.

Figures 1(a)–(f) display some key time stamps during the eruption of the jet at different passbands, with panels (a)–(c) from the EUV observations of AIA, panels (d) and (e) from the UV observations of IRIS (the green dashed lines represent the positions of the IRIS slits), and panel (f) from the EUV observations of SUTRI. Figure 1(a) depicts the first brightenings (green dashed box) at the footpoint region of the jet at around 15:12 UT, which marks the excitation of the plasma ejection. Figures 1(b) and (c) show the coronal responses of the jet body (red arrow) and its footpoint region at 15:20 UT, at the passband of 131 Å (∼10 MK in flaring regions) and 171 Å (∼0.6 MK). The brightenings at different passbands in the footpoint regions of solar jets are widely believed to be signatures of various scales of magnetic reconnections (e.g., R. L. Moore et al. 2010). The

curved structures in the footpoint region are essentially miniature flare loops, which usually form a shape of inverse-"Y" or "λ" with the jet spire. From the online animation of Figure 1, one can observe the whole process of the jet eruption and find the curtain-like shape of the jet body. This is a typical observational feature of the so-called "blowout" jets (e.g., R. L. Moore et al. 2010; Y. Shen et al. 2012; A. C. Sterling et al. 2015), which are results of minifilament (magnetic flux rope (MFR)) eruptions. The jet also exhibits apparent rotational motion (clockwise when seeing from above), which is also widely suggested as a manifestation of the untwisting motion of the MFR after the magnetic reconnection (e.g., Q. Zhang et al. 2012; J. Liu et al. 2017; N. C. Joshi et al. 2018). Both the post-reconnection loops and the jet body are visible in Figures 1(a)–(f), suggesting that the plasma of the jet and its footpoint region have a wide temperature distribution from the transition region to the hot corona.

Figure 1(g) presents the normalized average intensity in the region enclosed by the green dashed box in Figure 1(b) across different passbands of SDO/AIA, IRIS/SJI, and SUTRI. These curves show the responses of the jet eruption in passbands over a temperature range from 0.05 MK to at least several million kelvin, again confirming the multithermal nature of the jet. It is worth noting that almost all passbands show simultaneous increases and decreases in intensity, indicating rapid responses of the plasma temperature during magnetic reconnection and the subsequent cooling process. At least two jet eruptions are visible in the normalized curves between 15:00 and 16:00 UT. In this work, we focus on the first one, which is bigger in terms of spatial size and emission responses.

Figure 2(b) shows the time–distance diagram along the jet spire (red line in Figure 2(a)) in the AIA 304 Å passband using the *sunslice* code[7] developed by us (J. Liu 2026). The widths between the white solid lines represent the slice widths, which are 10 and 25 pixels, respectively. Combined with Figure 1(g), it can be observed that there are two prominent eruptions, occurring around 15:20 and 15:40 UT, interspersed with intermittent ejections known as subjets (J. Liu et al. 2014). The dashed lines represent the projected axial speed of the jet on the plane of sky (POS), and the velocities of both jets are around 300 km s^{-1}, faster than many solar jets observed, which have an average speed of 200 km s^{-1} (e.g., Y. Shen 2021). It can also be found from Figure 2(b) that the entire eruption process lasts approximately 40 minutes. Figure 2(c) displays the time–distance diagram of the first jet in the direction perpendicular to its main axis (blue line in Figure 2(a)), revealing apparent lateral motion toward the south side. The lateral motion, namely the whipping motion, is a typical feature of solar jets, manifesting the reconfiguration of the magnetic field lines during the magnetic reconnection (e.g., T. Yokoyama & K. Shibata 1995; R. C. Canfield et al. 1996). The lateral velocity of the jet in the diagram is found to be on the order of 5–6 km s^{-1}. Besides the lateral motion, the first jet also shows apparent rotational motions (a typical characteristic of blowout jets). To investigate the line-of-sight (LOS) Doppler velocities induced by the rotational motion of the jet, we conducted observations using the IRIS "sit-and-stare" mode in the Si IV λ1403 spectral line (green dashed line in Figure 1(d)). Figure 3(a) shows the intensity map of the jet in the IRIS Si IV λ1403 line, where a series of continuous bright features are observed to evolve over time. The LOS Doppler velocity map, derived from the following formula, is presented in Figure 3(b):

$$v_{\rm Dop} = I_{\rm line}^{-1} \int (I_{\rm obs} - I_{\rm min})\, dv_{\rm los}, \tag{1}$$

where $I_{\rm obs}$ represents the observed intensity measured by the spectrograph and $I_{\rm min}$ denotes the minimum value of $I_{\rm obs}$. The main body of the jet exhibits distinct redshift and blueshift signals in the Doppler velocity map, with a clear north–south dichotomy: redshifts dominate the northern part, while blueshifts prevail in the south. To this end, we applied yet another feature tracking algorithm (B. Welsch & D. Longcope 2003; C. DeForest et al. 2007) to isolate these reliable signals, which are significantly above the background noise. The detected blueshift signals, outlined by the color contours in Figure 3(c), have an average velocity of $v_b = 26.9 \pm 1.4$ km s^{-1}. The corresponding redshift signals, displayed in Figure 3(d), average $v_r = 37.2 \pm 0.5$ km s^{-1}. The observed blueshift and redshift Doppler velocities are a result of the combined LOS component of the jet's rotational and axial motions. A larger blueshift Doppler velocity than the redshift Doppler velocity indicates that the jet axis is inclined toward the observer away from the solar surface. Its rotational speed is then estimated as $v_r = \frac{1}{2}(v_b + v_r) = 32.1 \pm 0.9$ km s^{-1}.

3. DEM and Energy Analysis

The six optically thin AIA emission passbands are used to determine the DEM distribution. These passbands contain contributions from different ionization states of iron, specifically 94 Å (Fe X, Fe XVIII), 131 Å (Fe VIII, Fe XXI), 171 Å (Fe IX), 193 Å (Fe XII, Fe XXIV), 211 Å (Fe XIV), and 335 Å (Fe XVI). These passbands are sensitive to plasma within a temperature range of 10^5–10^7 K. Although the AIA 304 Å passband was used in the previous section to illustrate the dynamics of the jet, it is optically thick and therefore not suitable to be used in the DEM analysis.

The DEM represents the integral of the plasma emission in a specific temperature interval along the LOS and is expressed as follows:

$$\mathrm{DEM}(T) = n(T)^2 \frac{dh}{dT}, \tag{2}$$

where $n(T)$ denotes the electron number density at temperature interval $(T, T + dT)$ along the LOS with a depth of h. We applied the regularization inversion technique developed by M. Hahn et al. (2011) to reconstruct the DEM distribution for each pixel from the six AIA EUV passbands, covering a temperature range from 0.2 to 32 MK. By integrating the DEM over this temperature range, the total emission measure (EM) is obtained via

$$\mathrm{EM} = \int \mathrm{DEM}(T) dT. \tag{3}$$

According to X. Cheng et al. (2012) and K. Vanninathan et al. (2015), the average temperature can be calculated using the weighted DEM (X. Cheng et al. 2012; K. Vanninathan et al. 2015):

$$\overline{T} = \frac{\int \mathrm{DEM}(T)\, T\, dT}{\mathrm{EM}}. \tag{4}$$

[7] https://github.com/PyDL/sunslice/

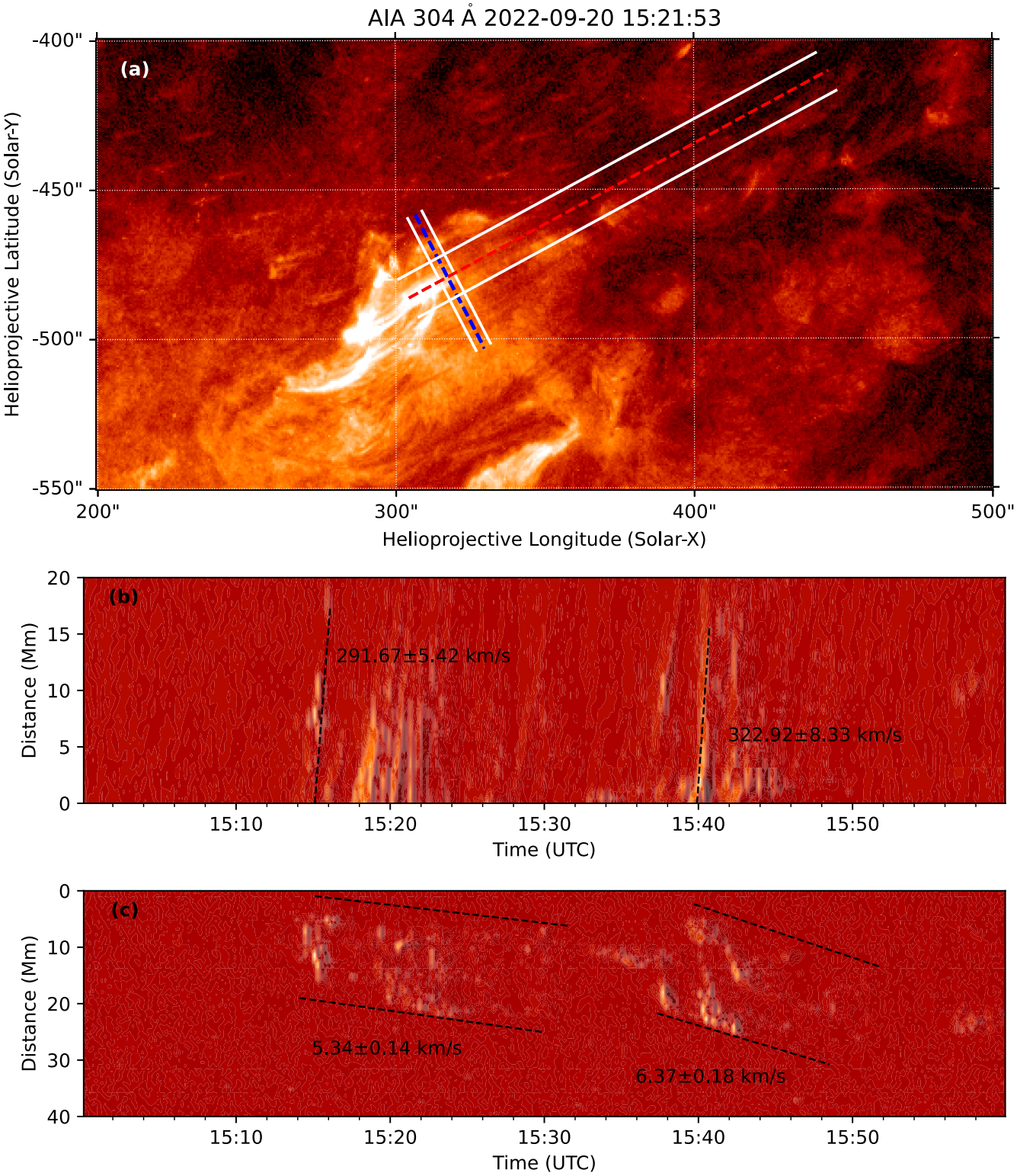

Figure 2. Time–distance diagram in the AIA 304 Å passband. Panel (a) shows the slices along the axial and perpendicular directions of the jet. The lengths and widths of the slices are determined by the lengths of the dashed lines and the distance between the two white solid lines, respectively. The width of the axial slice is 25″, and the width of the perpendicular slice is 10″. Panels (b) and (c) display the time–distance diagrams along the axial and perpendicular directions of the jet, respectively, with the estimated velocities marked by the black dashed lines.

Figure 4 shows the DEM distribution at the temperature range of 0.5–32 MK during the jet eruption at 15:22 UT. The logarithm of the DEM ranges from 19 to 23 cm^{-5} K^{-1}. The flare loop at the jet's footpoint region is visible at a temperature between 4.0 and 19 MK (Figures 4(f)–(j)), showing the high-temperature nature of the flare loop associated with the jet eruption. When the temperature exceeds 19 MK (Figures 4(k)–(l)), the high-temperature emission is confined to the footpoints of the flare loop and the base of the jet, with no signature detected at the loop top. The main body

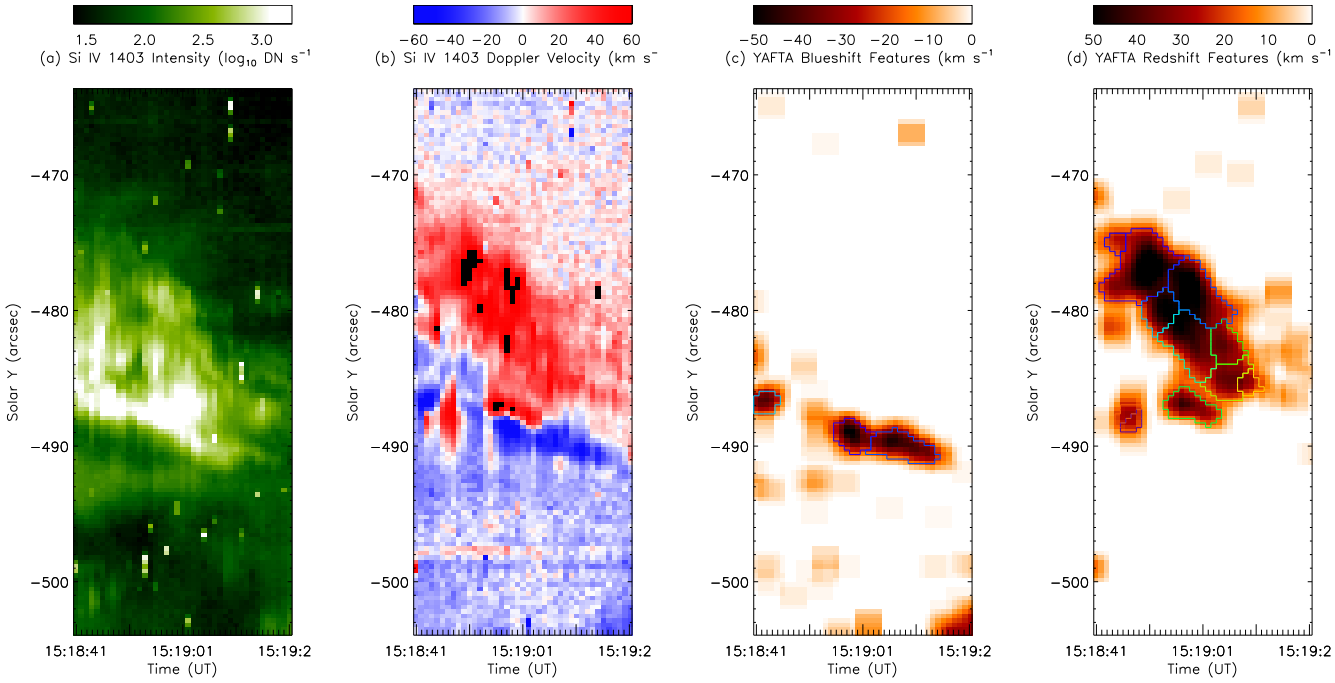

Figure 3. Spectral observation of jet at IRIS Si IV λ1403. (a), (b) Zeroth and first moments of IRIS Si IV λ1403, respectively. (c), (d) YAFTA feature detection results from the blueshifted and redshifted parts of panel (b), respectively. Colored contours surround the detected features, which are significantly larger than the background noise.

of the jet shows a wider existence and is visible across the whole temperature range, again revealing the multithermal nature of the jet plasma. Comparing Figure 4(a) with Figures 4(g)–(l), one can find that the cold (<1 MK) component of the jet has a width of around $10''$ at its base, which is attached to the flare loop, while the hot (>6 MK) component has a width of only around $2''$ and is detached from the flare loop. These differences in the spatial and thermal distribution of the jet plasma are consistent with the theory that many solar jets result from (cold) minifilament eruptions, with some of the plasma heated to higher temperatures by the interchange magnetic reconnection between the closed and open magnetic field lines (A. C. Sterling et al. 2016).

Figure 5(a) shows the weighted temperature of the flare loop and the jet at 15:22 UT. Very high temperatures, around 20 MK, can be found at the two footpoint regions of the flare loops and at the base of the jet body. These are consistent with the scenario that the jet is triggered by the interchange magnetic reconnection between closed loop systems and open magnetic field lines, which directly heats plasma at the reconnection region (jet base), and extra heating can be found at the loop footpoint regions owing to the chromospheric evaporation by the reconnection-accelerated particles. The flare loops and the rest of the jet body (the jet spire) also show high temperatures around 10 MK. These temperatures are clearly much higher than those of the background corona (around 1 MK).

We further calculated the temperature variations of the jet and the loop, as shown by the red and blue regions in Figure 5(a). From Figure 5(b), it can be seen that the temperatures of the jet and the loop begin to increase simultaneously around 15:12 UT. The loop temperature exhibits two distinct peaks, with the first peak occurring at 15:17:23 UT. As shown in the AIA 94 Å channel image (panel (d)), compared with the onset of the eruption (15:13:23 UT, panel (c)), the red region brightens significantly at 15:17:23 UT. This enhancement is likely caused by magnetic reconnection between the magnetic loop and the background open magnetic field. By 15:21:47 UT (panel (e)), a distinct flare-like circular structure can be clearly seen, and the temperature of the magnetic loop reaches its maximum value. The loop is heated almost simultaneously with the jet body, though its temperature is slightly higher than that of the jet plasma, indicating that the loop released energy during the eruption and strongly heated the jet's footpoint region. The maximum temperature of the jet is approximately $(1.0 \pm 0.3) \times 10^7$ K, while the maximum temperature of the loop is about $(9.3 \pm 1.1) \times 10^6$ K. After 15:22 UT, both temperatures decrease simultaneously and eventually stabilize at around 4.0×10^6 K.

Knowing the jet's thermal and dynamical properties, we can estimate its thermal and kinetic energies. The length (l) of the jet spire is estimated to be approximately 25.09 ± 0.08 Mm, and the average width (w) is about 4.42 ± 0.19 Mm. If we consider the jet as a cylinder (which is usually true according to previous observations; e.g., J. Liu et al. 2014), the volume (V) of the jet is calculated to be approximately $(3.85 \pm 0.33) \times 10^{20}$ m^3. The axial velocity (v) of the jet, obtained from the time–distance diagram in Figure 2(a), is approximately 291.7 ± 5.4 km s^{-1}. And the rotational speed of the jet is found to be around 32.1 ± 0.9 km s^{-1}. The kinetic energy can then be calculated using the formula $E_k = 0.5mv^2$. Here v is the speed norm combining the axial speed and the rotational speed; m is the mass of the jet, which is $n \cdot \overline{\mu} \cdot V$, with $\overline{\mu}$ the average molecular weight of the jet plasma and n the plasma number density. The velocity v is defined to represent the bulk (mass transport) flow speed of the jet plasma. The small transverse swaying motion discussed earlier is not included in the kinetic energy estimation, not only because its amplitude is small but also for clear physical reasons. First, the transverse swaying velocity is much

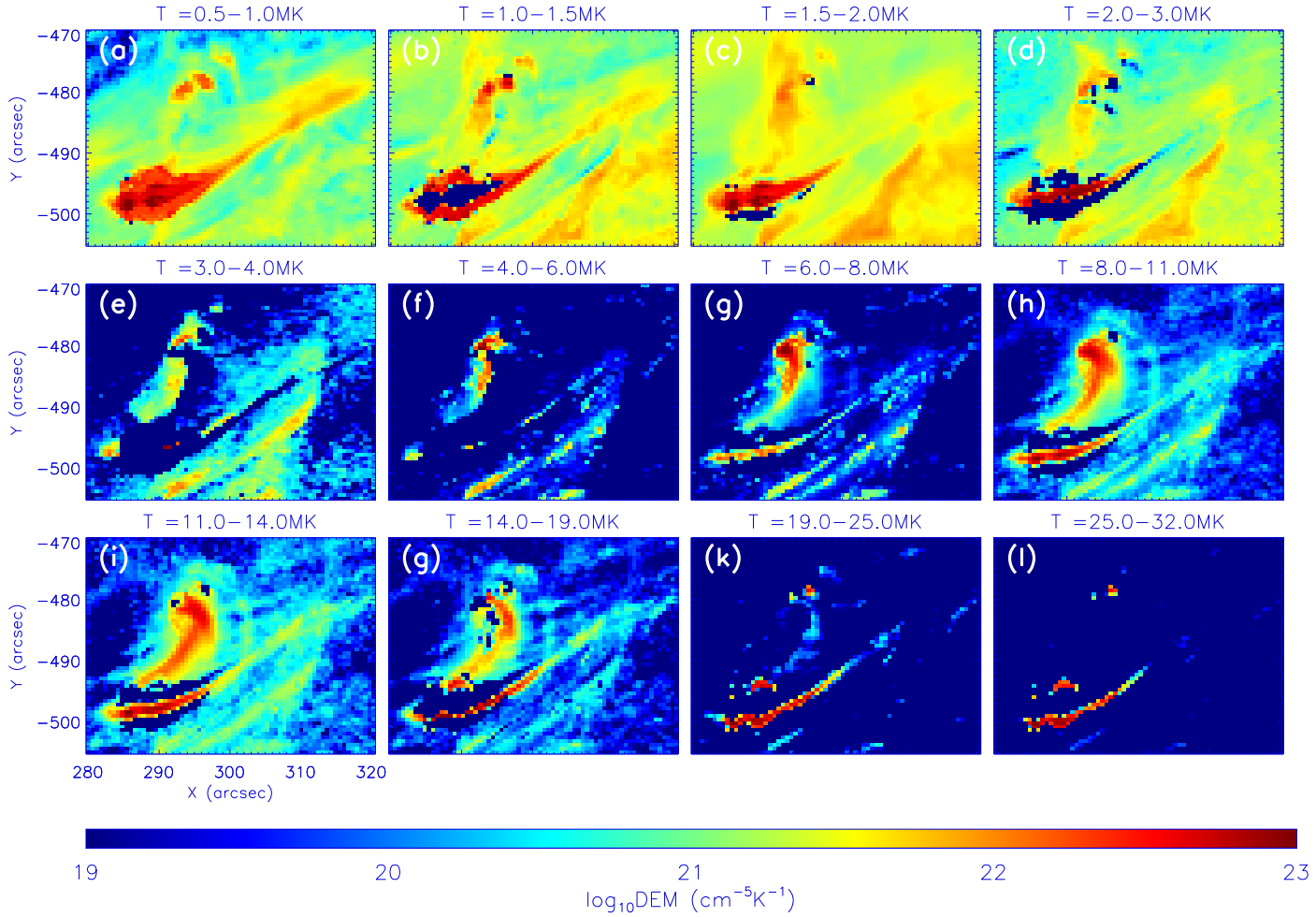

Figure 4. DEM distribution of the jet and its footpoint region at 15:22 UT across different temperature intervals, ranging from 0.5 to 32 MK with 0.5 MK intervals. The DEM range is from 10^{19} to 10^{23} cm^{-5} K^{-1}.

smaller than both the axial and rotational components, and since the kinetic energy scales with the square of velocity, the contribution from this swaying motion is expected to be negligible and within the measurement uncertainties. Second, the observed swaying is more likely a manifestation of a transverse oscillation or wavelike displacement of the jet axis, consistent with a kink-mode perturbation, rather than a sustained net transverse mass transport. Therefore, our estimation focuses exclusively on the kinetic energy associated with the jet's bulk axial outflow and rotational motion. Since hydrogen is the main component of the Sun, the molecular mass of the jet is taken as the mass of a hydrogen atom, $\overline{\mu} = 1.67 \times 10^{-27}$ kg. The plasma number density is derived from $n = \sqrt{\frac{EM}{h}}$, where h is the column depth of the emitting plasma along the LOS and equals the average width w of the jet spire given the assumption that the jet spire resembles a cylinder. EM is the average emission measure in the blue region at the time indicated by the blue line in Figure 5(b), which is $(8.3 \pm 7.2) \times 10^{28}$cm^{-5}, and the average plasma number density can be estimated as $(1.94 \pm 0.84) \times 10^{16}$ m^{-3}. Taking all the above parameters into account, the kinetic energy of the jet is then estimated to be approximately $(5.4 \pm 2.4) \times 10^{20}$ J.

Assuming that the jet plasma conforms to the ideal gas laws, the thermal energy could be estimated using the ideal gas internal energy formula $Q = \frac{3}{2}nVkT$, where k is the Boltzmann constant. The temperature (T) used here is the average temperature in the blue region at the time indicated by the blue line in Figure 5(b), which is about 0.63×10^7 K. Taking this into account, the thermal energy of the jet could be estimated as $(7.0 \pm 3.6) \times 10^{20}$ J. Despite the relatively large errors (∼50%) introduced during the above estimations, the jet's thermal and kinetic energies are roughly on the same order, obeying the equipartition law of jet energies found by J. Liu et al. (2016). The jet's total energy (sum of the thermal and kinetic energies) is on the order of 10^{21} J (10^{28} erg), falling into the range of coronal jets' thermal energies (10^{27}–10^{29} erg) estimated in J. Liu et al. (2023a) using only SDO/AIA 304 Å observations, with a total number of more than 1200 coronal jets.

4. Magnetic Field Topology

In this section, we investigate the relationship between the jet eruption and the topology and evolution of the photospheric magnetic field obtained. Figures 6(a) and (b) show the images of the jet in the AIA 304 Å and AIA 1600 Å passbands, respectively. The green dashed boxes represent the footpoint region of the jet (same as the green dashed box in Figure 1(a)), where apparent brightening can be observed in both passbands, again indicating the wide temperature response down to the upper photosphere. The contours of the simultaneous LOS

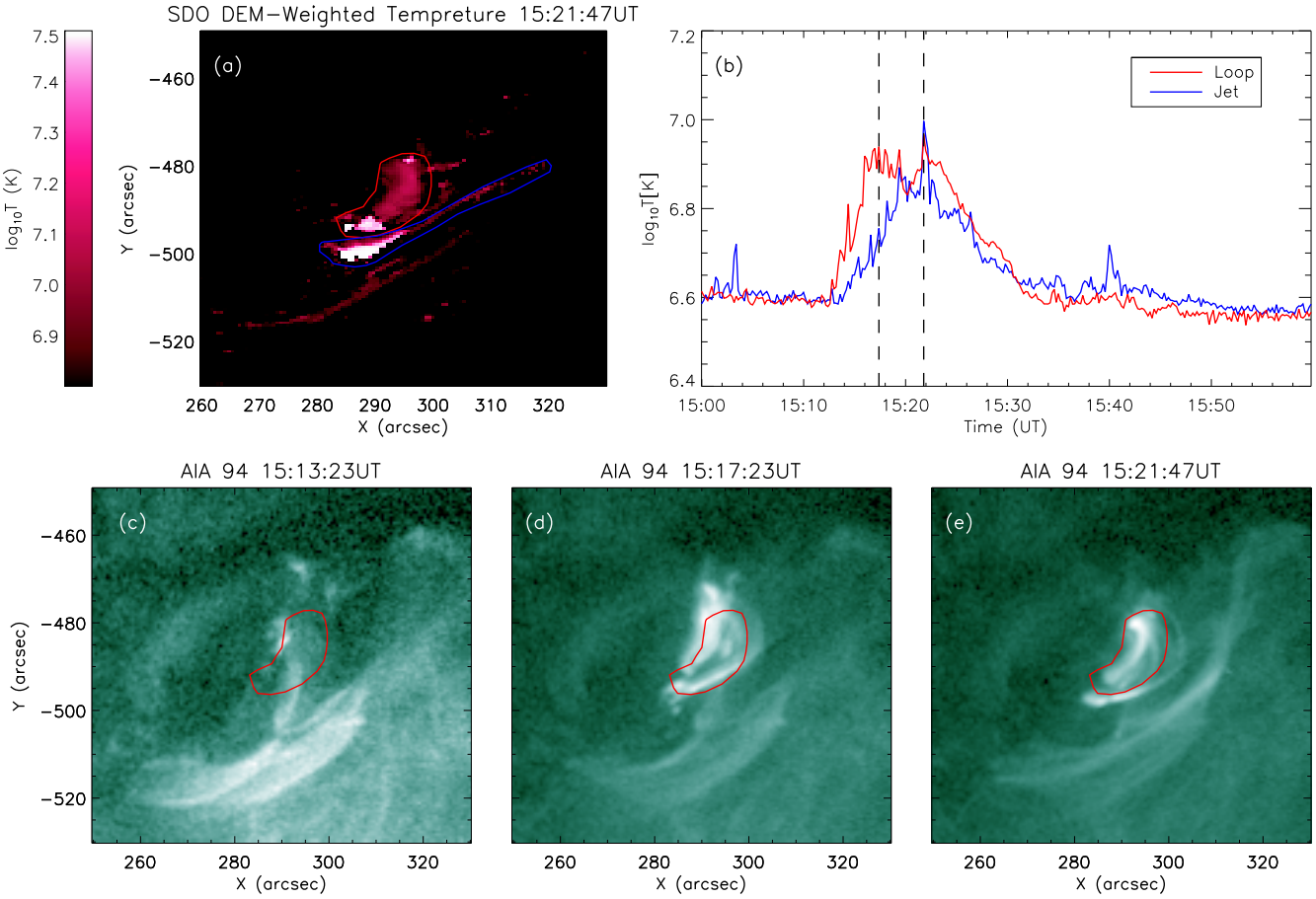

Figure 5. (a) SDO DEM-weighted temperature map at 15:21:47 UT, where the region enclosed by the red curve represents the footpoint loop system and the region enclosed by the blue curve represents the jet. (b) The time evolution of the average temperature for the two regions, with the black dashed line indicating the time of the local maximum value of the curves. (c)–(e) The AIA 94 Å images at the onset of the eruption and at the two times marked by the vertical dashed lines in panel (b) are shown. The red contours correspond to the same region as in panel (a).

magnetic field are overlaid on the images, with red representing the positive polarity and blue representing the negative polarity. Clearly, the jet eruption corresponds to a complicated small region at the edge of the AR with multiple mixed polarities.

Subsequently, we analyze the LOS magnetic field in the footpoint region of the jet. After alignment and normalization, the temporal variation of the total negative LOS magnetic flux, total positive LOS magnetic flux, total net LOS magnetic flux, and total unsigned LOS magnetic flux in the green box in Figure 6(a) are shown as curves of different colors in Figure 6(d), respectively. The orange and blue curves in Figure 6(c) represent the normalized AIA 304 Å and AIA 1600 Å intensities in the region enclosed by the green box, respectively. The total negative LOS magnetic flux (Figure 6(d)) shows a continuous increase before the end of the first jet (indicated by recovery to the background level of the AIA 304 Å intensity at approximately 15:30 UT). The total positive LOS magnetic flux, in contrast, shows a continuous decrease before the first jet erupts. These suggest that the jet eruption should be related to the flux emergence of the negative polarities in the region surrounded by the green box in Figure 6(a), which can also be confirmed by investigating the online movie related to Figure 1. This process of emerging negative polarities is also reflected in the decreasing net LOS magnetic flux, as shown in Figure 6(d). The total net LOS magnetic flux and the unsigned LOS magnetic flux show a "U" shape before and during the jet eruption. This may suggest that the magnetic reconnection could be related to the magnetic flux cancellation process, which is a common phenomenon during the eruption of solar jets (e.g., Y. Jiang et al. 2007; R. A. McGlasson et al. 2019; S. Patsourakos & V. Archontis 2025). The subsequent increase in both positive and unsigned flux suggests flux emergence or redistribution after the eruption, contributing to the post-eruptive magnetic recovery.

To further study the magnetic topology at the jet's footpoint regions, a series of HMI vector magnetic field data are obtained from the Spaceweather HMI Active Region Patch (SHARP; M. G. Bobra et al. 2014; J. T. Hoeksema et al. 2014). Figure 7 depicts the vertical component (B_z) in the vector magnetograms from 8:00 UT (before the jet eruption) to 16:00 UT (after the jet eruption), with overlaid horizontal velocity fields, showing the temporal evolution of the magnetic field at the jet's footpoint region. The green box in Figure 7(a) encloses the same area as the green boxes in Figure 1. From 11:00 UT, the positive polarity on the east (P0) continuously fragments into small positive polarities, which then converge to create the small polarity *P* (Figure 7(b)). Meanwhile, the positive polarity *P* moved closer to the negative polarity *N*, gradually forming an area with magnetic neutral lines, as indicated by the white arrows in Figures 7(b)–(f). From 11:00 to 15:12 UT, the apparent size of the negative polarity *N* grows continuously, corresponding to the increase of the total

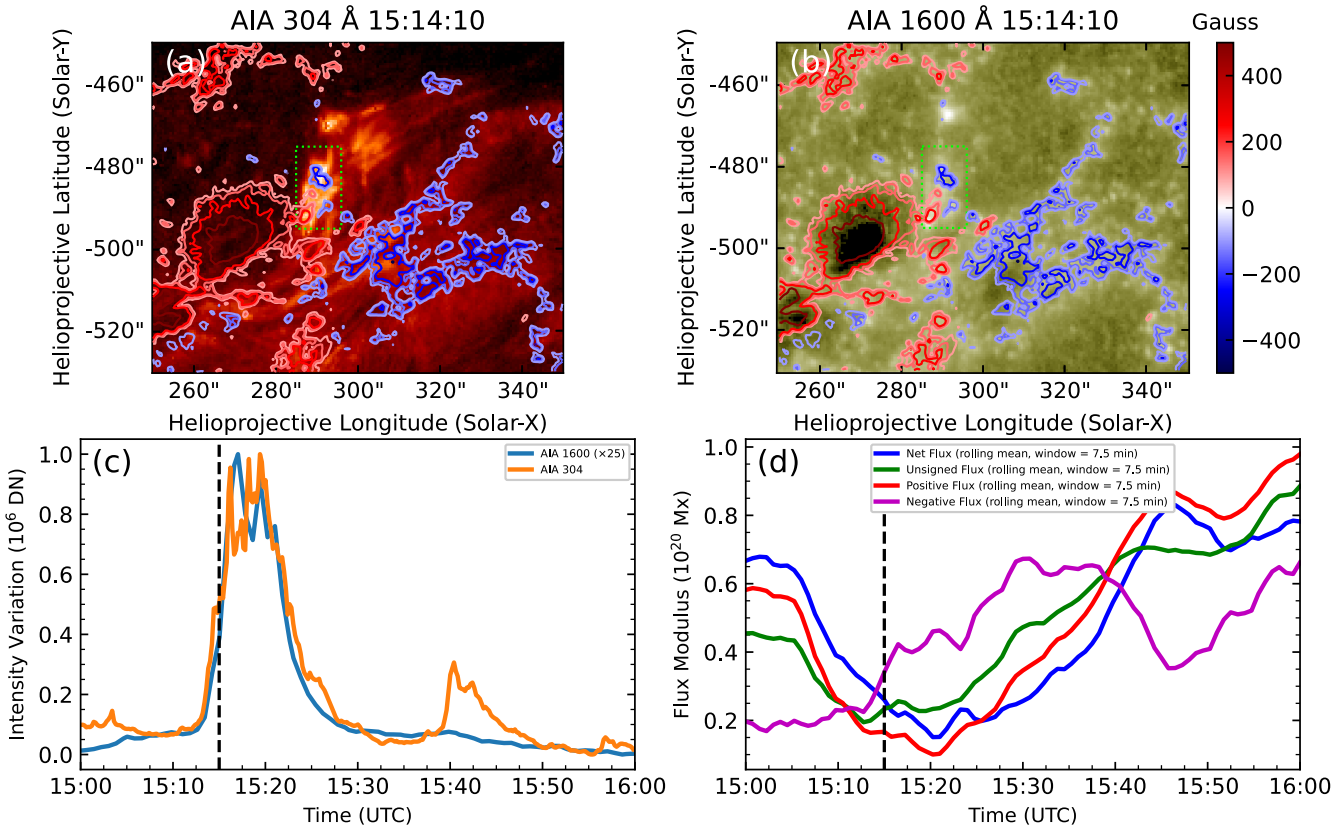

Figure 6. Panels (a) and (b) show the AIA 304 and 1600 Å observations, respectively, overlaid with the LOS magnetic field distribution at 15:14:10 UT. The red and blue contours represent the ranges of ±500 G, respectively, and the green dashed box is the same as the green dashed box in Figure 1(a), indicating the jet footpoint region. Panel (c) displays the intensity variation curves for AIA 304 and 1600 Å, with the dashed line marking the moment of the jet initiation. Panel (d) shows the time variation curves of the modulus of the total positive magnetic flux, the modulus of the total negative magnetic flux, the modulus of the total net magnetic flux, and the modulus of the total unsigned magnetic flux, with units of Mx. The dashed line corresponds to the same moment as in panel (c).

negative flux in Figure 6(c), and eventually leads to the eruption of the jet. From 15:24 UT, the negative polarity N starts to move away from the positive polarity P, begins to merge with a bigger negative polarity at its north, and eventually deforms most of the magnetic neutral line (16:00 UT in Figure 7(i)). Arrows in Figures 7(b)–(f) point to the region of the magnetic neutral line, which corresponds well in space with the location between the jet and the flare loops, as shown in Figure 1(b). This again provides evidence of the causal relationship between the evolution of the photospheric magnetic field topology and the eruption of the jet.

To investigate the magnetic topological structure of the jet footpoint region and explore how the jet erupts, we apply the nonlinear force-free field (NLFFF) extrapolation method (T. Wiegelmann 2008) to the HMI photospheric vector magnetic field before and after the jet eruption. This method is based on the minimum dissipation theory and satisfies the force-free field and torque-free conditions. Since the photosphere is not necessarily force-free, the photospheric magnetic field is smoothed and preprocessed before being used as the boundary condition of the 3D magnetic field extrapolation. The coronal magnetic field is then extrapolated using an optimization-based NLFFF solver, in which the magnetic field is iteratively relaxed by minimizing a functional that enforces both the force-free and solenoidal constraints within a Cartesian computational domain. A multigrid optimization implementation is employed (executed via the `multigrid` solver), with three multigrid levels (level = 3) and a computational volume of $n_x \times n_y \times n_z$, where $n_z = 256$. A boundary buffer layer of thickness $n_d = 32$ pixels is applied, and a weighting mask proportional to the normalized transverse field strength ($B_T/\max(B_T)$) is adopted to down-weight weak-field regions on the boundary. The HMI/SHARP vector magnetograms are preprocessed before extrapolation (executed via `multiprepro`) to reduce the net force and torque and to smooth the boundary (e.g., T. Wiegelmann et al. 2006; T. Wiegelmann & T. Sakurai 2021). Based on the extrapolation results, the twist number (T_w) and squashing factor (Q) are also calculated using the method by R. Liu et al. (2016). The twist number (T_w) represents the number of winding turns between two magnetic field lines with an indefinitely close distance, and its specific formula is as follows (e.g., M. A. Berger & C. Prior 2006; R. Liu et al. 2016):

$$T_w = \frac{1}{4\pi}\int_0^l \alpha dl. \quad (5)$$

Here α represents the force-free factor and l is the length of the target magnetic field line. The squashing factor (Q) quantifies the divergence of neighboring magnetic field lines, helping to identify complex structures and topological features in the solar magnetic field, which are critical to determine the location where the magnetic reconnection might happen. Details of how the squashing factor is calculated and its application in finding MFRs in the solar atmosphere can be found in R. Liu et al. (2016).

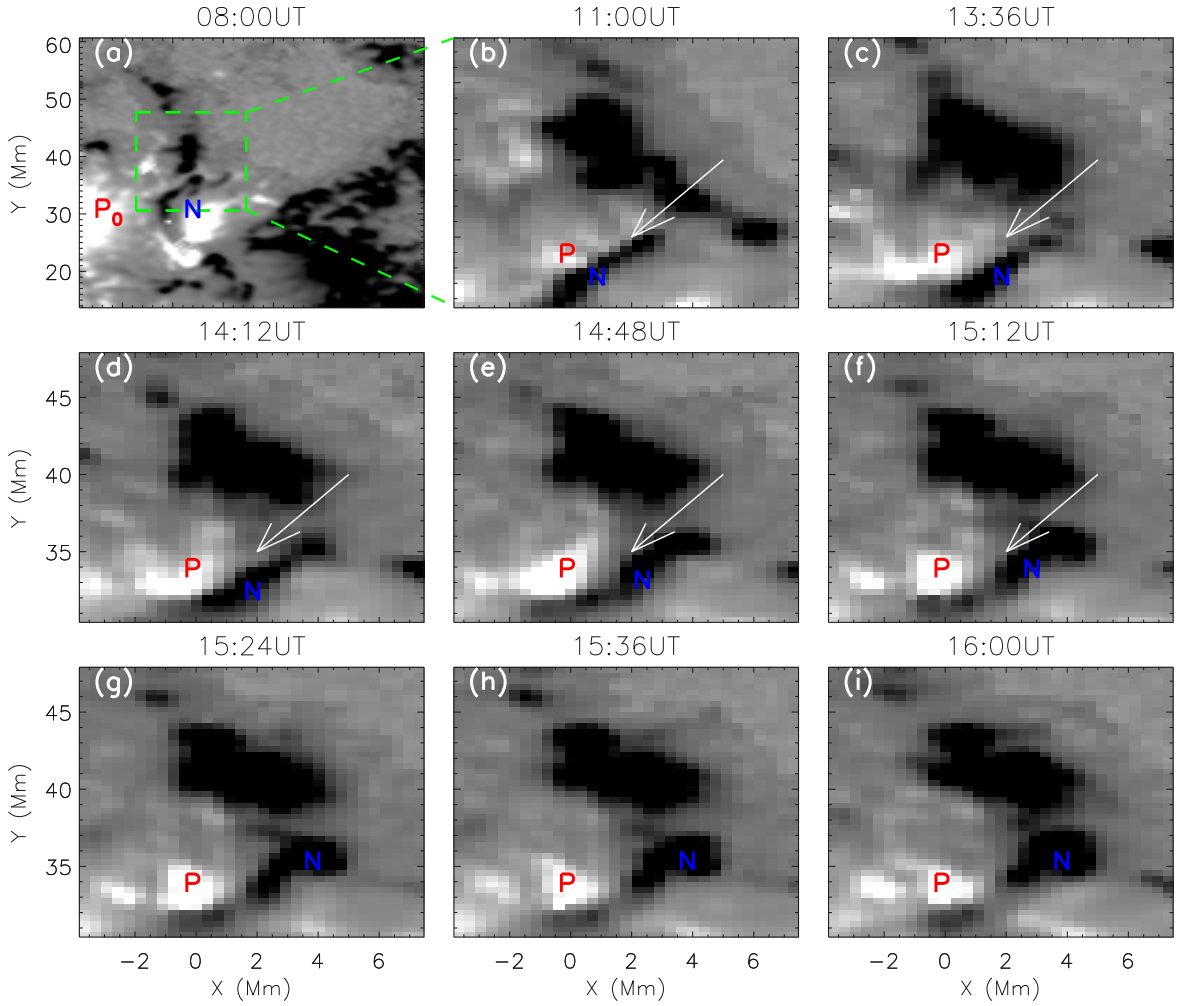

Figure 7. Evolution of the photospheric vertical magnetic field. In panel (a), the green dashed box represents the jet footpoint region, which is located in the same position as the green dashed box in Figure 1(a). N represents the negative polarity in the footpoint region, and P_0 represents the positive polarity located southeast of the footpoint region. Starting from 8:00 UT, P_0 continuously splits into smaller positive polarities, which move toward N and eventually merge into the positive polarity P. The white arrow indicates the location of the polarity inversion line.

Figure 8(a) shows the vertical magnetic field at 15:12 UT, right before the magnetic reconnection that triggers the jet starts. The green dashed box encloses the same region as the green dashed box in Figure 7. The horizontal red line is a slit that cuts through the magnetic neutral line and is roughly perpendicular to the local segment of the magnetic neutral line. Panels (b), (c), and (d) depict the magnetic field vector, the squashing factor Q, and the twist number T_w in the plane of the slit extending from the photosphere to a height of ∼11 Mm, respectively. An apparent structure with rotating magnetic field vectors, whose center is denoted by the green triangle, is visible in the lower right corner of Figure 8(b). The green triangle in Figure 8(a) indicates the location of the structure within the photospheric magnetic field, viewed from above. A region surrounded by significant Q factors is found around the structure in Figure 8(c). These are typical examples of evidence for the existence of an MFR, with the green triangle denoting the location of the MFR axis. Large twist numbers above 1 can be seen inside the MFR, with the green triangle located in the region with the most significant twist numbers. The largest twist number of the MFR is found to be around 2.1 (4.2π). This positive twist number is also consistent with the clockwise untwisting motion of the observed jet found from the IRIS spectral observations shown in Figure 3, given that the rotational motion of jets is widely believed as a result of the untwisting process of the MFR after the magnetic reconnection. Figure 8(e) shows the change of the maximum twist number of the MFR before, during, and after the jet eruption within a 3D volume. This volume is defined by extruding the horizontal area of the green dashed box in panel (a) vertically to a height of approximately 11 Mm. The continuous trend of the increasing twist number before the magnetic reconnection begins at 14:12 UT indicates the buildup of the free magnetic energy. The twist number decreases to below 2 immediately after the magnetic reconnection, suggesting a sudden release of the free magnetic energy corresponding to the jet eruption.

5. Summary and Discussion

In this paper we have presented the analysis of a multithermal coronal jet that occurred in AR 13102 on 2022 September 20 using multi-instrument observations from SDO/AIA, SDO/HMI, IRIS, and SUTRI. The combined EUV, UV, and magnetic diagnostics provide a comprehensive view of the jet's dynamic evolution, thermal structure, and magnetic environment.

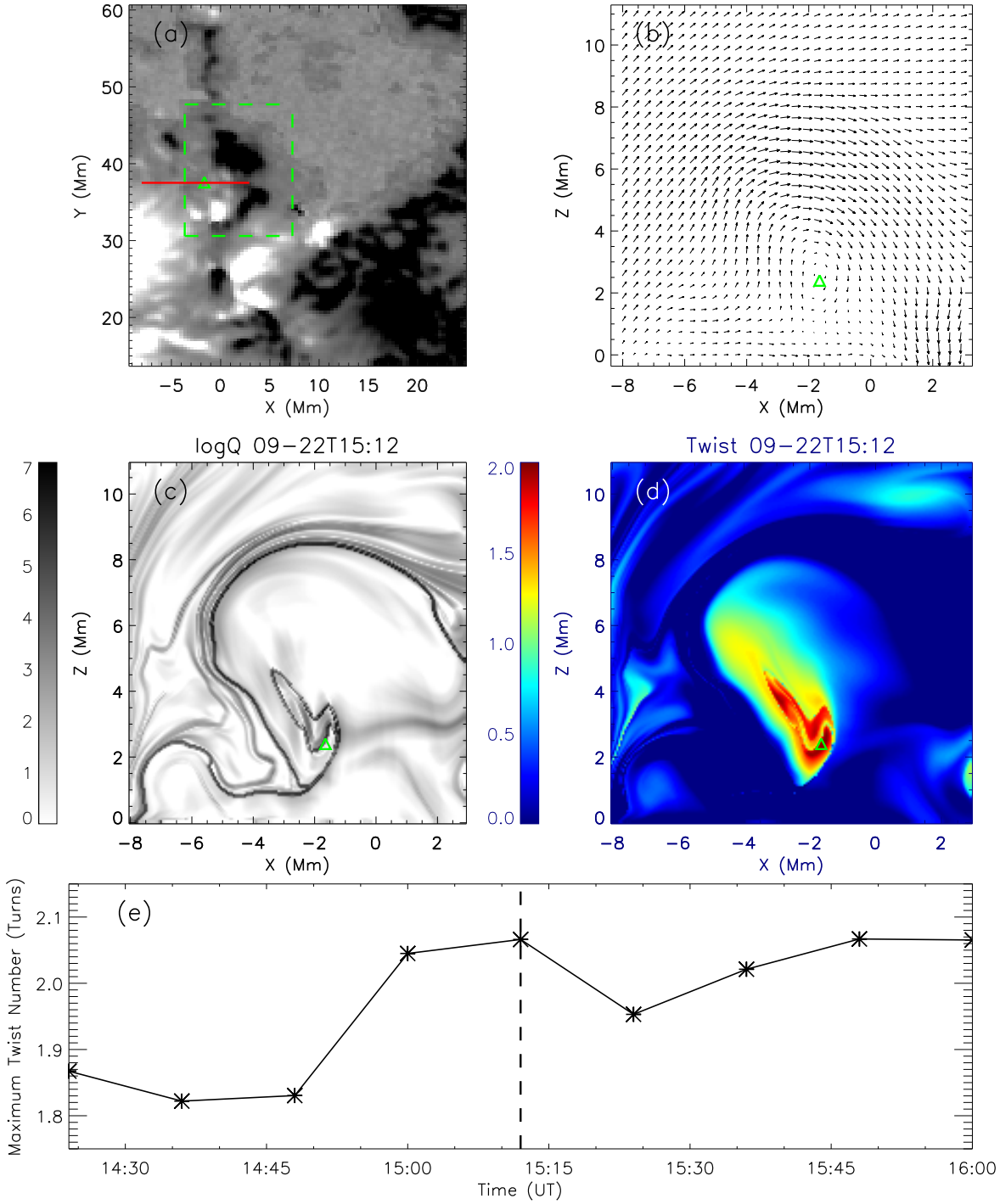

Figure 8. Panel (a) shows the vector magnetogram of the photosphere at 15:12 UT. The green dashed box marks the footpoint region of the jet, corresponding to Figure 1(a). The red line indicates the position of the slice, which is taken at $y = 37.52$ Mm with a length of ∼11 Mm. Panel (b) presents the horizontal magnetic field in the x–z plane, with the green triangle denoting the center of the identified MFR. Panels (c) and (d) display the distributions of the squashing factor and twist number, respectively, on the slice. Panel (e) shows the temporal evolution of the maximum twist number of the MFR in the jet footpoint region, with the dashed line indicating the onset time of the jet eruption.

The jet was initiated by compact brightenings at its footpoint, simultaneously detected in multiple passbands, indicating the presence of magnetic reconnections. In the early phase, the reconnection produced a miniature flare loop with an inverse-"Y" configuration, and the subsequent eruption formed a curtain-like spire—typical of blowout-type jets. The eruption displayed a broad temperature response—from ∼0.05 MK in the transition region to $\gtrsim$10 MK in the hot corona—demonstrating its strongly multithermal nature. The normalized intensity profiles from AIA, IRIS, and SUTRI show nearly synchronous brightenings, confirming rapid plasma heating followed by cooling during the reconnection process. The unique observations from SUTRI revealed a clear response of the jet and magnetic reconnection in the transition region. In the SUTRI 465 Å channel, a pronounced intensity enhancement is clearly observed cospatial with the jet footpoint, and its temporal evolution is highly consistent with that seen in the IRIS and AIA observations. As shown in

Figure 1, during the onset phase of the jet, the increase in intensity and the attainment of the peak value occur almost simultaneously, indicating a rapid and direct response of the transition region plasma to the magnetic reconnection process.

Kinematic analysis reveals both axial and rotational motions of the jet. The jet reached an axial velocity of ~300 km s^{-1} in the POS, higher than the average value for coronal jets, while IRIS Si IV λ1403 spectra exhibit opposite Doppler shifts of 30–40 km s^{-1} on the two sides of the jet, implying a clockwise rotation when seen from the top of the jet. A weak lateral displacement (~5 km s^{-1}) toward the south is also seen, which is often a direct result of the interchange slip-running reconnection. These kinematic signatures, together with the morphology, identify the event as a blowout jet, which is believed to be usually triggered by the eruption of a twisted MFR.

DEM analysis derived from the six AIA EUV channels shows that the jet plasma spans temperatures of 0.5–32 MK, with log DEM between 19 and 23 cm^{-5} K^{-1}. The hot component (>6 MK) is confined near the base and footpoints of the flare loops, whereas the cooler component (<1 MK) extends along the spire. Using the derived emission measure and density estimates, the kinetic and thermal energies were found to be $E_k \approx 5.4 \times 10^{20}$ J and $E_{\rm th} \approx 7.0 \times 10^{20}$ J, respectively. These comparable magnitudes suggest near-equipartition between kinetic and thermal energies, consistent with previous statistical results for coronal jets (e.g., J. Liu et al. 2016, 2023a).

Magnetic field analysis using HMI LOS and vector magnetograms reveals that the jet originated from a mixed-polarity region at the edge of the AR. Continuous flux emergence of negative polarity, accompanied by the decrease of positive flux, occurred before the eruption, leading to net flux reduction and suggesting the coexistence of flux emergence and cancellation. The vector field evolution exhibits converging movements between opposite polarities, promoting the formation of a sheared neutral line favorable for reconnection. NLFFF extrapolation further identifies a compact MFR at the jet's footpoint, with a maximum twist number $T_w \approx 2.1$ (4.2 π) and surrounded by a high-Q quasi-separatrix layer. The observed decrease in the twist number after the eruption indicates the sudden release of magnetic helicity and free magnetic energy, consistent with the observed untwisting motions and plasma acceleration.

Taken together, these observations support a coherent picture in which emerging and canceling magnetic flux in a small, mixed-polarity region drives reconnection between a twisted MFR and the surrounding open magnetic field, resulting in a blowout jet. In a future work, we will utilize advanced numerical simulations to explore more physics of this event, and the simulation must simultaneously reproduce the following observational constraints:

1. The presence of a compact flux rope rooted at the jet base and enclosed by a high-Q layer, with a twist number close to the kink instability threshold prior to eruption and a measurable decrease after the event.
2. Efficient plasma acceleration characterized by a high axial jet speed, substantial rotational motion across the spire, and a small but finite lateral drift consistent with slip-running interchange reconnection.
3. A strongly multithermal plasma response spanning ~0.5–32 MK, with the hottest component concentrated near the jet base and an energy partition in which the thermal energy is comparable to the kinetic energy.

These combined constraints link magnetic reconnection, flux rope eruption, and plasma acceleration and place quantitative limits on the energy release and helicity transport processes in small-scale solar eruptions.

The thermal energy of the jet estimated by the multi-wavelength observations is consistent with that calculated by only SDO/AIA 304 Å observations in the statistical analysis by J. Liu et al. (2023a). To further assess and calibrate the reliability of estimating coronal jet thermal energies from a single optically thick passband (AIA 304 Å), we will carry out a forthcoming Solar Cycle 24 coronal jet survey based on the more than 1000 events cataloged by J. Liu et al. (2023a). We will perform a direct event-by-event comparison between proxy energies inferred from AIA 304 Å alone and thermal energies derived from DEM analysis. The larger sample will enable a more meaningful calibration and a robust assessment of the associated uncertainties.

Acknowledgments

This research is supported by the National Natural Science Foundation (NSFC 12373056, 42188101, 42521007) and the Strategic Priority Research Program of the Chinese Academy of Sciences (grant No. XDB0560000) and China's Space Origins Exploration Program. SUTRI is a collaborative project conducted by the National Astronomical Observatories of CAS, Peking University, Tongji University, Xi'an Institute of Optics and Precision Mechanics of CAS, and the Innovation Academy for Microsatellites of CAS. We also acknowledge the use of the data from the Solar Dynamics Observatory (SDO). SDO is the first mission of NASA's Living With a Star (LWS) program. The SDO/AIA and SDO/HMI data are publicly available from NASA's SDO website (https://sdo.gsfc.nasa.gov/data/). IRIS is a NASA small explorer mission developed and operated by LMSAL, with mission operations executed at NASA Ames Research Center and major contributions to downlink communications funded by ESA and the Norwegian Space Centre. This research is also supported by the International Space Science Institute (ISSI) in Beijing.

Facilities: SDO (AIA, HMI), IRIS.

ORCID iDs

Chunyu Ji https://orcid.org/0009-0006-4430-7882
Jiajia Liu https://orcid.org/0000-0003-2569-1840
Wensi Wang https://orcid.org/0000-0002-9865-5245
Zhenyong Hou https://orcid.org/0000-0003-4804-5673
Xianyong Bai https://orcid.org/0000-0003-2686-9153
Yuming Wang https://orcid.org/0000-0002-8887-3919

References

Anfinogentov, S., Kaltman, T., Stupshin, A., Nakariakov, V., & Loukitcheva, M. 2021, STP, 7, 3
Bai, X., Tian, H., Deng, Y., et al. 2023, RAA, 23, 065014
Baikie, T. K., Sterling, A. C., Moore, R. L., et al. 2022, ApJ, 927, 79
Berger, M. A., & Prior, C. 2006, JPhA, 39, 8321
Bhatnagar, A., Prasad, A., Nóbrega-Siverio, D., van der Voort, L. R., & Joshi, J. 2025, A&A, 698, A174
Bobra, M. G., Sun, X., Hoeksema, J. T., et al. 2014, SoPh, 289, 3549
Bura, A., Samanta, T., Sterling, A., et al. 2025, ApJ, 983, 144
Canfield, R. C., Reardon, K. P., Leka, K., et al. 1996, in Magnetodynamic Phenomena in the Solar Atmosphere: Prototypes of Stellar Magnetic Activity (Springer), 49
Chandrashekhar, K., Bemporad, A., Banerjee, D., Gupta, G., & Teriaca, L. 2014, A&A, 561, A104

Cheng, X., Zhang, J., Saar, S., & Ding, M. 2012, ApJ, 761, 62
Cheung, M. C., De Pontieu, B., Tarbell, T. D., et al. 2015, ApJ, 801, 83
Chifor, C., Isobe, H., Mason, H., et al. 2008, A&A, 491, 279
Cirtain, J., Golub, L., Lundquist, L., et al. 2007, Sci, 318, 1580
De Pontieu, B., Title, A., Lemen, J., et al. 2014, SoPh, 289, 2733
DeForest, C., Hagenaar, H., Lamb, D., Parnell, C., & Welsch, B. 2007, ApJ, 666, 576
Duan, Y., Tian, H., Chen, H., et al. 2024, ApJL, 962, L38
Fang, F., Fan, Y., & McIntosh, S. W. 2014, ApJL, 789, L19
Hahn, M., Landi, E., & Savin, D. W. 2011, ApJ, 736, 101
Harrison, R., Bryans, P., & Bingham, R. 2001, A&A, 379, 324
Hoeksema, J. T., Liu, Y., Hayashi, K., et al. 2014, SoPh, 289, 3483
Hoshino, M., & Higashimori, K. 2015, JGRA, 120, 3715
Innes, D. E., Bučík, R., Guo, L.-J., & Nitta, N. 2016, AN, 337, 1024
Jiang, Y., Chen, H., Li, K., Shen, Y., & Yang, L. 2007, A&A, 469, 331
Joshi, N. C., Nishizuka, N., Filippov, B., Magara, T., & Tlatov, A. G. 2018, MNRAS, 476, 1286
Kayshap, P., Karpen, J. T., & Kumar, P. 2024, SoPh, 299, 88
Lemen, J. R., Title, A. M., Akin, D. J., et al. 2012, SoPh, 275, 17
Li, X., Keppens, R., & Zhou, Y. 2023, ApJL, 947, L17
Li, X., Solanki, S. K., Wiegelmann, T., et al. 2025, A&A, 702, A201
Li, X., Zhou, Y., & Keppens, R. 2025b, A&A, 698, A232
Lionello, R., Török, T., Titov, V., et al. 2016, ApJL, 831, L2
Liu, J. 2026, sunslice, v1, Zenodo, doi:10.5281/zenodo.18334987
Liu, J., Erdélyi, R., Wang, Y., & Liu, R. 2017, ApJ, 852, 10
Liu, J., Song, A., Jess, D. B., et al. 2023a, ApJS, 266, 17
Liu, J., Wang, Y., Erdélyi, R., et al. 2016, ApJ, 833, 150
Liu, J., Wang, H., et al. 2023b, ApJ, 945, 7
Liu, J., Wang, Y., Liu, R., et al. 2014, ApJ, 782, 94
Liu, R., Kliem, B., Titov, V. S., et al. 2016, ApJ, 818, 148
Loboda, I., Bogachev, S., Kirichenko, A., Reva, A., & Ulyanov, A. 2025, CosRe, 63, 23
Long, D. M., Chitta, L. P., Baker, D., et al. 2023, ApJ, 944, 19
Lu, L., Feng, L., Li, Y., et al. 2019, ApJ, 887, 154
Mandal, S., Chitta, L. P., Peter, H., et al. 2022, A&A, 664, A28
Masson, S., Pariat, E., Aulanier, G., & Schrijver, C. J. 2009, ApJ, 700, 559
McGlasson, R. A., Panesar, N. K., Sterling, A. C., & Moore, R. L. 2019, ApJ, 882, 16
Moll, R., Spruit, H., & Obergaulinger, M. 2008, A&A, 492, 621
Moore, R. L., Cirtain, J. W., Sterling, A. C., & Falconer, D. A. 2010, ApJ, 720, 757
Moore, R. L., Sterling, A. C., Falconer, D. A., & Robe, D. 2013, ApJ, 769, 134
Moore, R. L., Sterling, A. C., & Panesar, N. K. 2018, ApJ, 859, 3
Moreno-Insertis, F., & Galsgaard, K. 2013, ApJ, 771, 20
Murray, M. J., van Driel-Gesztelyi, L., & Baker, D. 2009, A&A, 494, 329
Narang, N., Arbacher, R. T., Tian, H., et al. 2016, SoPh, 291, 1129
Nisticò, G., Bothmer, V., Patsourakos, S., & Zimbardo, G. 2009, SoPh, 259, 87
Panesar, N. K., Hansteen, V. H., Tiwari, S. K., et al. 2023, ApJ, 943, 24
Panesar, N. K., Sterling, A. C., & Moore, R. L. 2016a, ApJL, 822, L23
Panesar, N. K., Sterling, A. C., Moore, R. L., & Chakrapani, P. 2016b, ApJL, 832, L7
Panesar, N. K., Sterling, A. C., Moore, R. L., et al. 2025, ApJ, 994, 164
Panesar, N. K., Tiwari, S. K., Moore, R. L., Sterling, A. C., & De Pontieu, B. 2022, ApJ, 939, 25
Patsourakos, S., & Archontis, V. 2025, A&A, 699, A87
Pesnell, W. D., Thompson, B. J., & Chamberlin, P. C. 2012, SoPh, 275, 3
Pike, C., & Mason, H. 1998, SoPh, 182, 333
Qi, Y., Huang, Z., Xia, L., et al. 2022, A&A, 657, A118
Sahay, A., Srivastava, A. K., et al. 2023, MNRAS, 521, 114
Samanta, T., Tian, H., Yurchyshyn, V., et al. 2019, Sci, 366, 890
Scherrer, P. H., Schou, J., Bush, R., et al. 2012, SoPh, 275, 207
Schmieder, B. 2022, FrASS, 9, 820183
Shen, Y. 2021, RSPSA, 477, 20200217
Shen, Y., Liu, Y., Su, J., & Deng, Y. 2012, ApJ, 745, 164
Shen, Y., Liu, Y. D., Su, J., Qu, Z., & Tian, Z. 2017, ApJ, 851, 67
Shibata, K., Ishido, Y., Acton, L. W., et al. 1992, PASJ, 44, 173
Shibata, K., Nakamura, T., Matsumoto, T., et al. 2007, Sci, 318, 1591
Shimojo, M., Hashimoto, S., Shibata, K., et al. 1996, PASJ, 48, 123
Sterling, A. C., Moore, R. L., Falconer, D. A., & Adams, M. 2015, Natur, 523, 437
Sterling, A. C., Moore, R. L., Falconer, D. A., et al. 2016, ApJ, 821, 100
Sterling, A. C., Moore, R. L., Falconer, D. A., Panesar, N. K., & Martinez, F. 2017, ApJ, 844, 28
Sterling, A. C., Moore, R. L., & Panesar, N. K. 2022, ApJ, 927, 127
Tan, S., Warmuth, A., Schuller, F., et al. 2025, A&A, 702, A189
Tian, H., DeLuca, E., Cranmer, S., et al. 2014, Sci, 346, 1255711
Touresse, J., Pariat, E., Froment, C., et al. 2024, A&A, 692, A71
Upendran, V., Tripathi, D., Vaidya, B., Cheung, M., & Yokoyama, T. 2025, ApJ, 985, 27
Vanninathan, K., Veronig, A., Dissauer, K., et al. 2015, ApJ, 812, 173
Wang, J., Lee, J., Chae, J., et al. 2024, ApJ, 974, 123
Welsch, B., & Longcope, D. 2003, ApJ, 588, 620
Wiegelmann, T. 2008, JGRA, 113, A03S02
Wiegelmann, T., Inhester, B., & Sakurai, T. 2006, SoPh, 233, 215
Wiegelmann, T., & Sakurai, T. 2021, LRSP, 18, 1
Wu, G., Yan, X., Xue, Z., et al. 2025, ApJ, 993, 171
Wyper, P. F., Antiochos, S. K., & DeVore, C. R. 2017, Natur, 544, 452
Yang, L., Peter, H., He, J., et al. 2017, ApJ, 852, 16
Yokoyama, T., & Shibata, K. 1995, Natur, 375, 42
Young, P. R., & Muglach, K. 2014, PASJ, 66, S12
Zhang, Q., Chen, P., Guo, Y., Fang, C., & Ding, M. 2012, ApJ, 746, 19
Zhang, Y., Musset, S., Glesener, L., Panesar, N. K., & Fleishman, G. D. 2023, ApJ, 943, 180